Supplementary Information (SI) for Journal of Materials Chemistry A.

Supporting Information

Embedding Zn Single-Atom Catalysts into Pyrrolic-N Defect Enriched Multilayer Carbon Sheets Boosts Sulfur Redox Kinetics

Cuiying Lu[a] , *Xiaoting Wang*[b], *Songjie He*[b], *Pei Chen*[b], *Siyu Liu*[b], *and Juan Yang*[b]*

[a] Shaanxi Key Laboratory of Low Metamorphic Coal Clean Utilization, School of Chemistry and Chemical Engineering, Yulin University, Yulin 719000, China

[b] School of Chemical Engineering and Technology, Xi'an Jiaotong University, Xi'an 710049, P. R. China

E-mail: juanyang@xjtu.edu.cn

Experimental Section

Materials: Zinc chloride ($ZnCl_2$), urea, sulfur (S), polyvinylidene fluoride (PVDF), N-methyl pyrrolidone (NMP), conductive carbon blacks, 1,3-dioxolane (DOL) and 1,2 dimethoxyethane (DME). All chemicals are analysis grade and can be directly used without further purification.

Material Characterization: The crystal structures of all the samples were collected by X-ray diffraction (XRD, Bruker D8 advanced). Raman spectra were taken by using RAMAN DXR2xi with the 532 nm excitation wavelength. X-ray photoelectron spectroscopy (XPS) was carried out on a Thermo Scientific K-Alpha$^+$ instrument with Al Kα radiation to analyze the chemical compositions. Scanning electron microscopy (SEM, MAIA3 LMH) and transmission electron microscopy (TEM, JEOL JEM-F200) were performed to observe the microstructural and morphological features of samples. The nitrogen absorption-desorption examinations were conducted with Micromeritics ASAP 2460. Ultraviolet-visible (UV-vis) absorbance spectroscopy of Li_2S_6 adsorption tests was investigated by UV-2600 variable wavelength spectrophotometer. The content of Zn species in the Zn-NMPC-5 was determined by Inductively coupled plasma optical emission spectroscopy (ICP-OES, Perkin Elmer 8300).

Polysulfide Redox Conversion: The sample (NMPC or Zn-NMPC-*x*, carbon black, and polyvinylidene fluoride (PVDF) with a mass ratio of 7:2:1 were grounded in N-methyl pyrrolidone (NMP) to form a homogeneous slurry and then coated on Al foil as electrode materials. The symmetric cells were assembled using identical electrodes as the working and counter electrodes, Celgard 2500 as the separator, and 40 μL Li_2S_6 (0.2 M) solution was used as electrolyte. Cyclic voltammogram (CV) measurements were examined between -1.0 and 1.0 V at different scan rates to evaluate polysulfide redox conversion kinetics.

Li_2S Nucleation and Dissociation Test: The preparation of the Li_2S_8 solution was similar to that of the Li_2S_6 electrolyte, except for Li_2S and S at a mass ratio of 1:7. The above electrode materials, Celgard 2500 and lithium foil were employed as cathodes, separator, and anode, respectively. 20 μL Li_2S_8 (0.2 M) as catholyte and 20 μL LiTFSI electrolyte without Li_2S_8 as the anolyte. For the nucleation of Li_2S, the assembled cells were firstly galvanostatically discharged at -0.112 mA to 2.06 V, followed by potentiostatically discharged at 2.04 V until the current decreased to 0.01 mA. After that, the cells were potentiostatically charged at 2.35 V until the current was below 0.01 mA for the Li_2S dissolution measurement.

Electrochemical Measurements: For the preparation of sulfur electrodes, 80 wt% NMPC@S or Zn-NMPC-*X*@S composites, 10 wt% carbon black, and 10 wt% PVDF were mixed in NMP and cast on aluminum foil and then dried in a vacuum oven at 60 °C for 12 h. The sulfur loading is about 1.0 mg cm^{-2}. The high sulfur loading electrodes were prepared by CNTs and Zn-NMPC-5@S composites. The coin cells (CR2016) were assembled using the as-obtained sulfur electrode as the cathode, Li foil as the anode, and modified commercial PP membrane (Celgard 2500) as the separator in an Ar-filled glovebox. A solution of LiTFSI (1.0 M) with 1.0 wt.% $LiNO_3$ dissolved in a solvent mixture of DOL and DME (1:1 in volume) as the electrolyte. The galvanostatic charge/discharge (GCD) curves, rate capacities, and cycling performances of batteries were operated on LAND2001A with a voltage window of 1.7-2.8 V. CV and electrochemical impedance spectroscopy (EIS) measurements were recorded on Bio-Logic VSP workstation. The EIS frequency range was from 0.01 Hz to 100 kHz.

Theoretical Calculation Details:

Density functional theory (DFT) computations were carried out by using the Vienna ab initio simulation package (VASP).[1] The projector-augmented wave approach (PAW) was used to describe the interaction between the ionic core and valence electrons.[2] The electron exchange and correlation energy were performed using the Perdew-Burke-Ernzerhof (PBE) function of generalized gradient approximation (GGA).[3] A vacuum separation of over 20 Å was employed to eliminate interactions between two adjacent unit cells. The first Brillouin Zone was sampled with k-point meshes of $3 \times 3 \times 1$ and $6 \times 6 \times 2$ for geometric optimization and self-consistent field (SCF) method, respectively. Considering the van der Waals (vdW) interactions, we adopted Grimme's semiempirical DFT-D3 scheme of dispersion correction. A kinetic energy cutoff of 400 eV for plane-wave basis was employed in all the calculations. The total energy convergence and the force convergence were set to lower than 1×10^{-5} eV and 0.02 eV/Å.

The d-band center was calculated by using the following equations:

$$\varepsilon_d = \frac{\int_{-\infty}^{0} n_d(\varepsilon)\varepsilon d\varepsilon}{\int_{-\infty}^{0} n_d(\varepsilon) d\varepsilon}$$

where ε is the electronic energy of states, and *n* is the electronic density of states.

The binding energy (E_b) of the polysulfides on G-N, Zn SAC, or Zn SAC-pyrrole N substrate was calculated using the equation:

$$E_b = E_{system} - E_{sub} - E_{Li_2S_n}$$

where E_{sub}, $E_{Li_2S_n}$ and E_{system} are the energies of the clean substrate, isolated Li_2S_n, and the polysulfide adsorbed on the corresponding substrate, respectively.

The simulation of the sulfur reduction reaction (SRR) process is challenging because of the difficulty of identifying the SRR equilibrium potential and the intermediate species. Current understanding mostly focuses on thermodynamics without including the electron contribution in the energy calculation.[4, 5] In this work, combined with our experimental measurements, we use the theoretical equilibrium potential to mimic the SRR process.[6] The SRR process includes 16 e^- conversions from bulk S_8 to bulk Li_2S and the possible reaction mechanisms are as follows [6, 7]:

$$S_8 + 2Li^+ + 2\,e^- + * \rightarrow Li_2S_8^*$$

$$Li_2S_8^* + \frac{2}{3}Li^+ + \frac{2}{3}e^- + \frac{1}{3} * \rightarrow \frac{4}{3}Li_2S_6^*$$

$$\frac{4}{3}Li_2S_6^* + \frac{4}{3}Li^+ + \frac{4}{3}e^- + \frac{2}{3} * \rightarrow 2\,Li_2S_4^*$$

$$2\,Li_2S_4^* + 4\,Li^+ + 4\,e^- + 2 * \rightarrow 4\,Li_2S_2^*$$

$$4\,Li_2S_2^* + 8\,Li^+ + 8\,e^- + 4 * \rightarrow 8\,Li_2S^*$$

$$8\,Li_2S^* \rightarrow 8\,Li_2S + 8 *$$

For the overall SRR:

$S_8 + 16\,Li^+ + 16\,e^- \rightarrow 8\,Li_2S$

the formation energy (E_f) of Li_2S is defined by

$E_f = 8E^{bulk}_{Li_2S} - E^{bulk}_{S_8} - 16E^{bulk}_{Li}$

and the $E^{bulk}_{Li_2S}$, $E^{bulk}_{S_8}$, and E^{bulk}_{Li} represent the energies of bulk Li_2S, S_8, and Li_1 (Li atom in bulk Li).

After full optimization, the total energies of -33.902 eV, -1.963 eV, and -12.587 eV for bulk S_8, Li_1 and Li_2S were obtained, respectively. The energy of $Li^+ + e^-$ at potential U = 0 is equal to that of Li_1.[8] Therefore, the formation energy of Li_2S and equilibrium potential U_0 are as follows:

$E_f = -35.389\ eV$

$U_0 = -E_f/16e = -(-35.389\ eV)/16e = 2.21V$

Supporting Figures and Tables

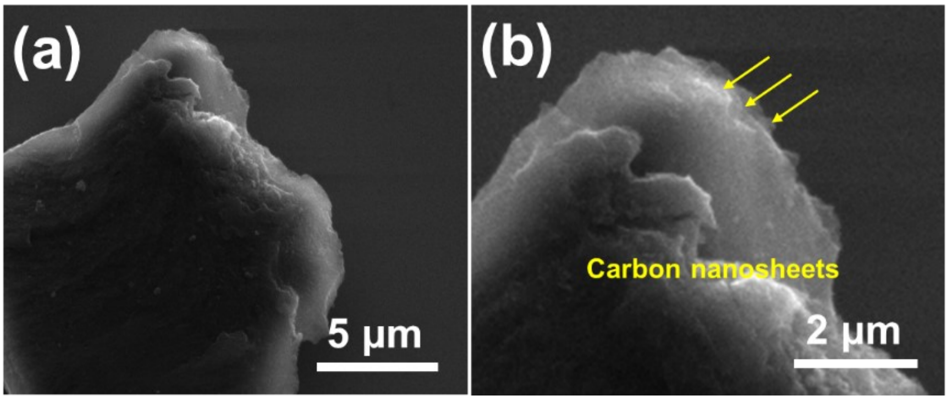

Fig. S1. (a, b) SEM images of the Zn-NMPC-1 sample.

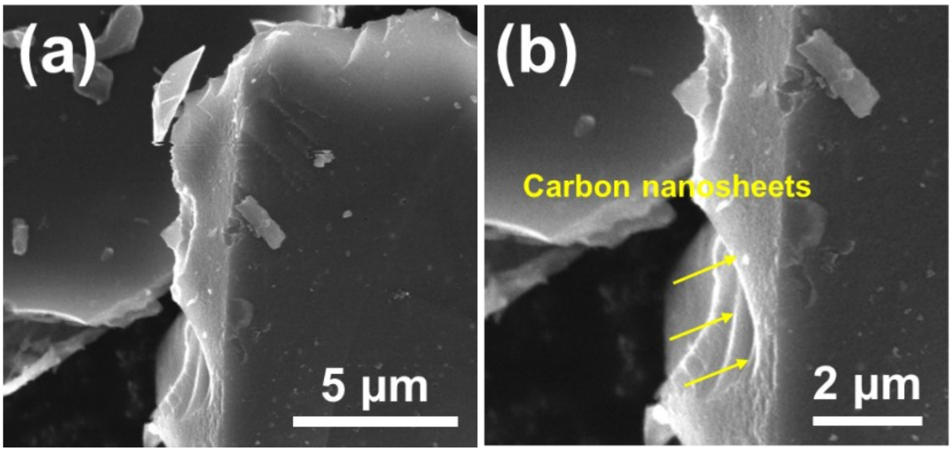

Fig. S2. (a, b) SEM images of the Zn-NMPC-10 sample.

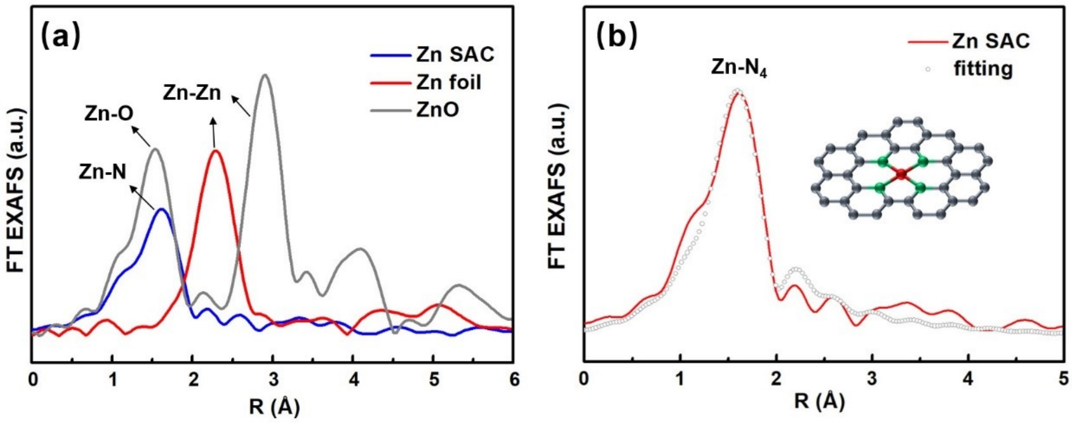

Fig. S3. (a) Fourier transforms of k2-weighted EXAFS spectra, (b) EXAFS fitting curves in R-space of Zn SACs obtained in the presence of $ZnCl_2$, which was demonstrated in previous work [9].

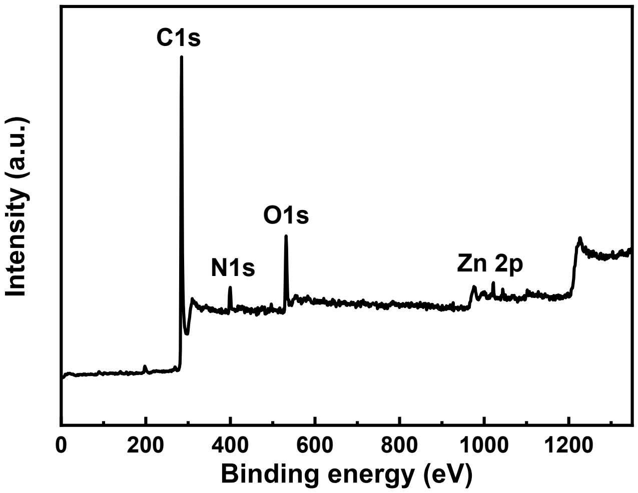

Fig. S4. XPS survey spectra of Zn-NMPC-5.

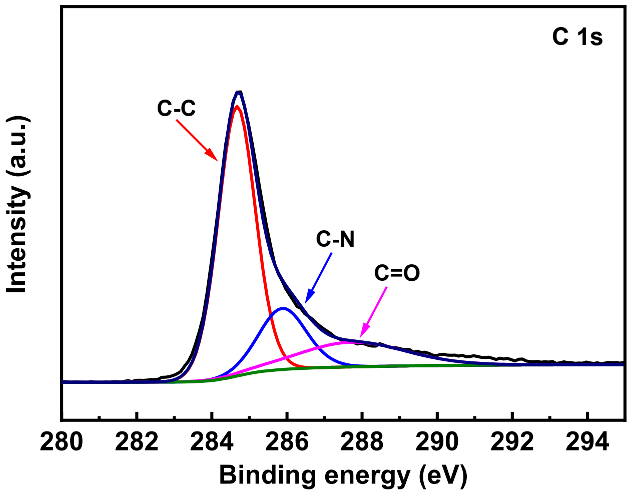

Fig. S5. XPS C 1s spectra of Zn-NMPC-5.

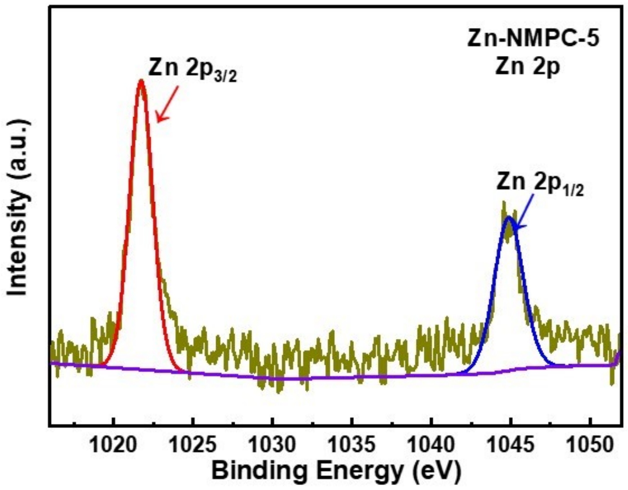

Fig. S6. High-resolution Zn 2p XPS spectra of Zn-NMPC-5.

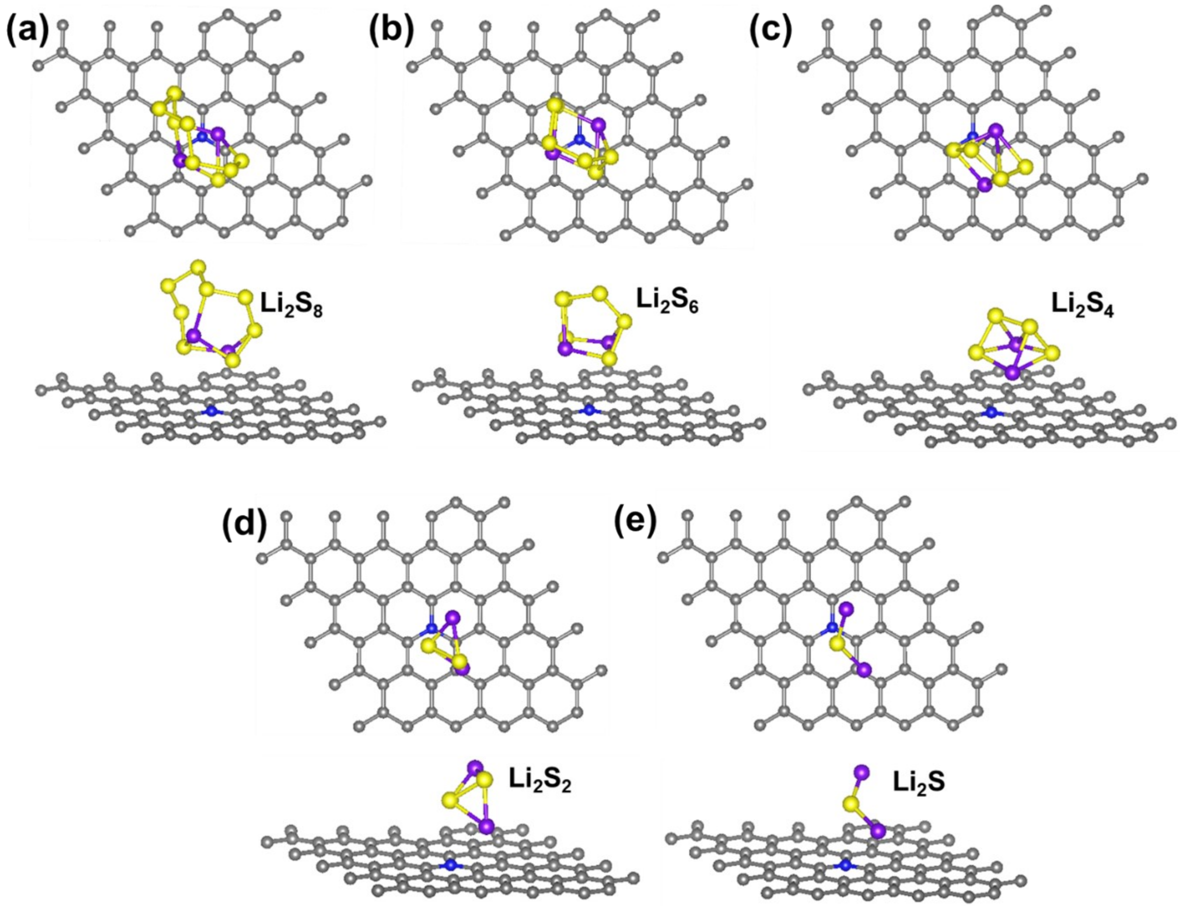

Fig. S7. The optimized adsorption conformations of different sulfur species on G-N. (a) Li_2S_8, (b) Li_2S_6, (c) Li_2S_4, (d) Li_2S_2, and (e) Li_2S. The gray, blue, purple, and yellow balls represent C, N, Li, and S atoms, respectively.

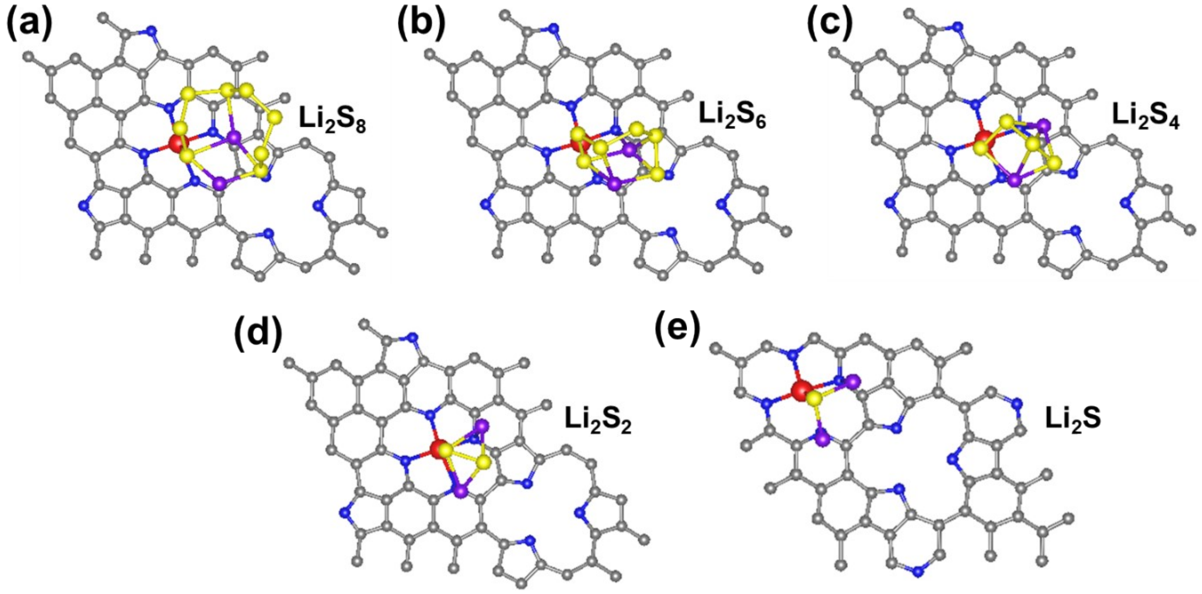

Fig. S8. The optimized adsorption conformations of different sulfur species on the Zn SACs-pyrrN surface. (a) Li_2S_8, (b) Li_2S_6, (c) Li_2S_4, (d) Li_2S_2, and (e) Li_2S. The gray, blue, purple, and yellow balls represent C, N, Li, and S atoms, respectively.

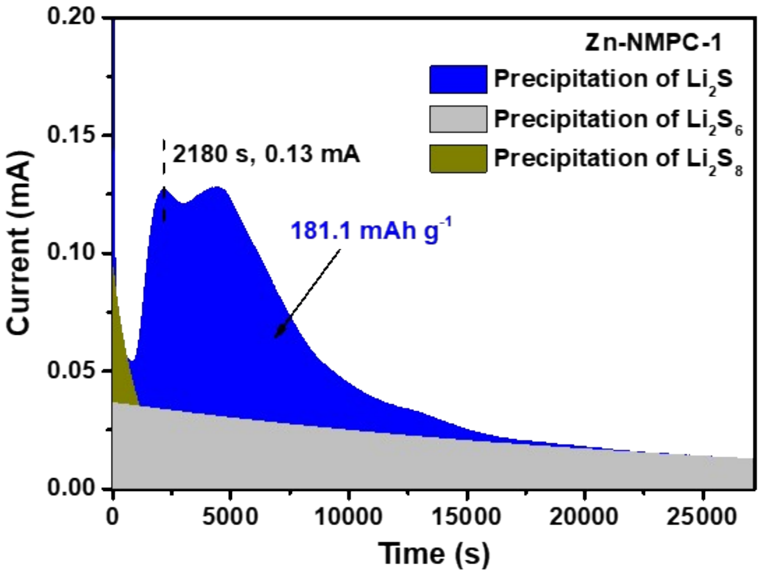

Fig. S9. Potentiostatic discharge profiles of Zn-NMPC-1 in Li_2S_8 solution at 2.04 V.

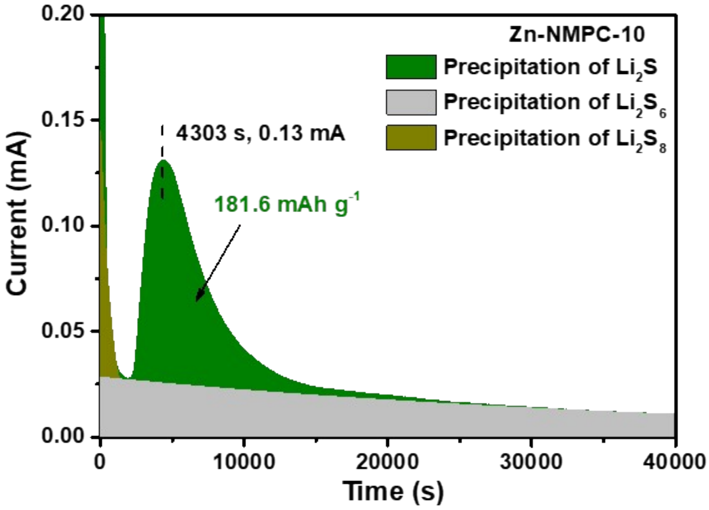

Fig. S10. Potentiostatic discharge profiles of Zn-NMPC-10 in Li_2S_8 solution at 2.04 V.

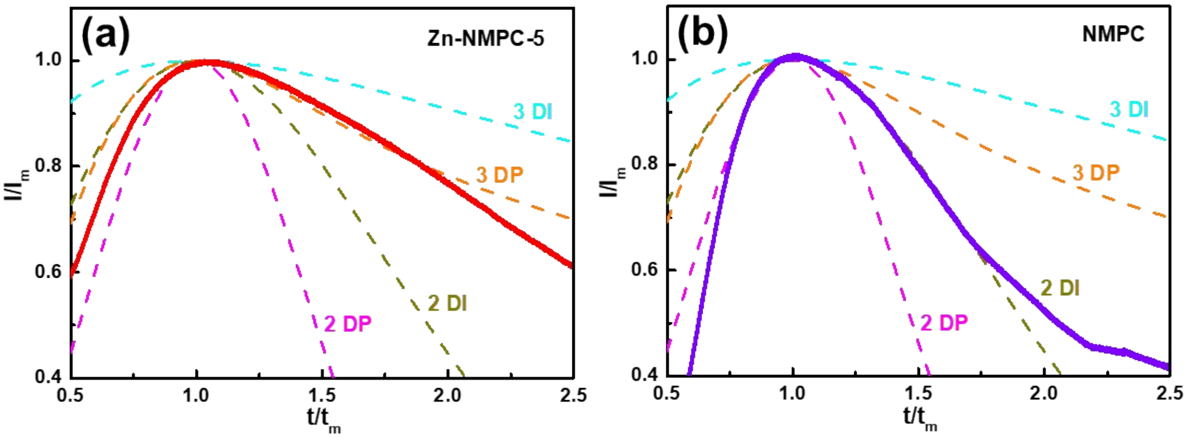

Fig. S11. Dimensionless transient curves of (a) Zn-NMPC-5 and (b) NMPC compared with theoretical models. Note: The nucleation rates of two-dimensional progressive nucleation (2DP) and instantaneous deposition (2DI) are controlled by the crystal phase, while the nucleation rates of three-dimensional progressive nucleation (3DP) and instantaneous deposition (3DI) are mainly determined by ion diffusion.

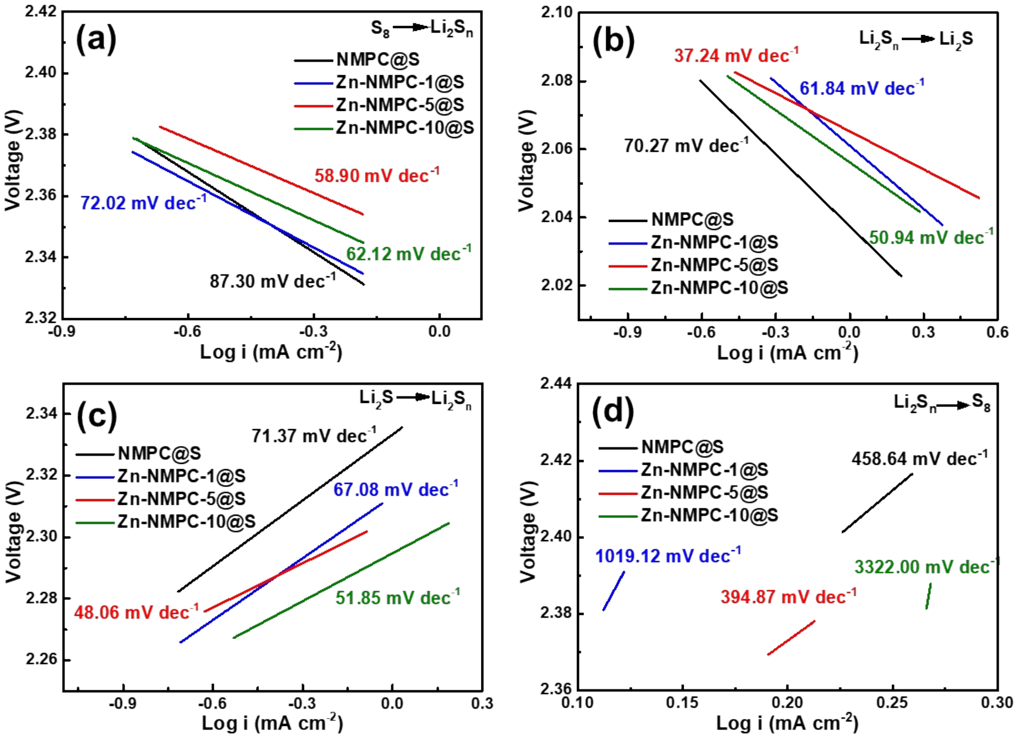

Fig. S12. Tafel plots from (a) S_8 to Li_2S_n, (b) Li_2S_n to Li_2S, (c) Li_2S to Li_2S_n and (d) Li_2S_n to S_8

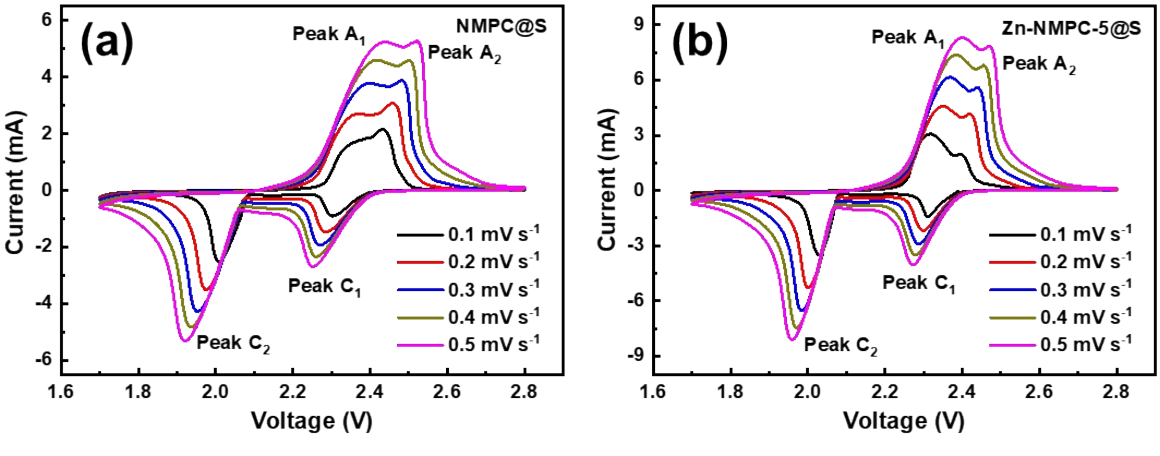

Fig. S13. CV profiles of (a) NMPC@S and (b) Zn-NMPC-5@S cathodes at scan rate from 0.1 mV s^{-1} to 0.5 mV s^{-1}.

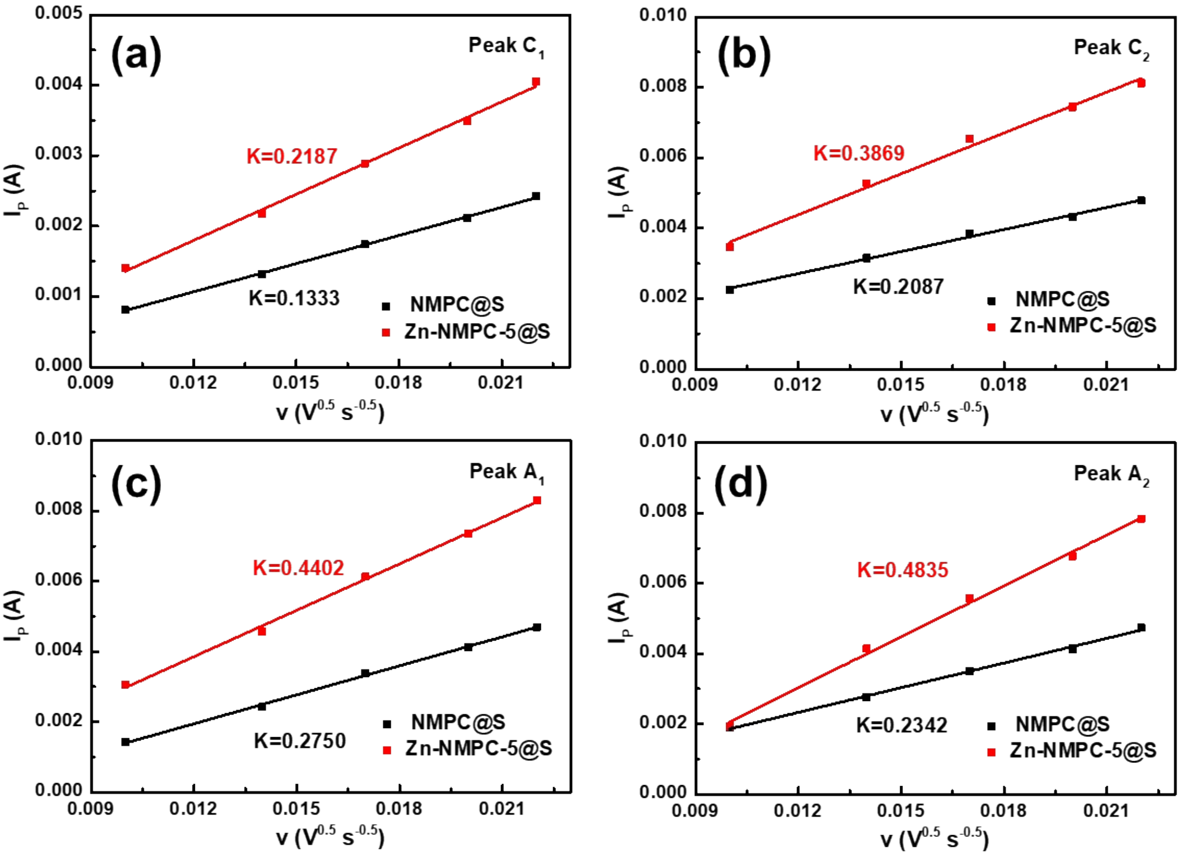

Fig. S14. The linear fitting of peak current and square root of the scan rates of NMPC@S and Zn-NMPC-5@S cathodes at (a) peak C_1, (b) peak C_2, (c) peak A_1, and (d) peak A_2.

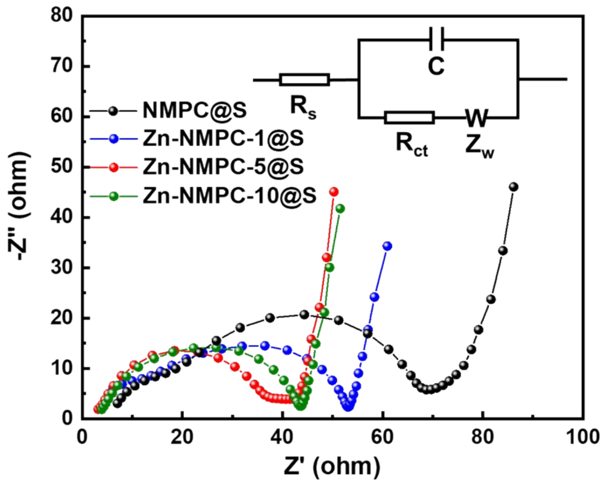

Fig. S15. EIS profiles of Li-S batteries with NMPC@S, Zn-NMPC-1@S, Zn-NMPC-5@S, and Zn-NMPC-10@S cathodes.

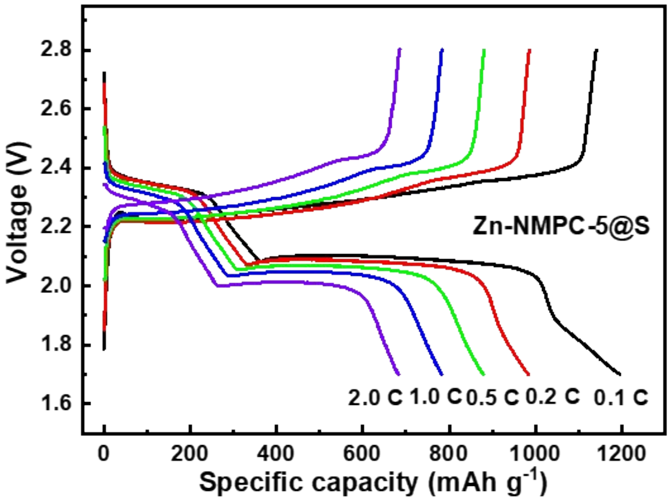

Fig. S16. The GCD curves of Zn-NMPC-5@S at various current rates.

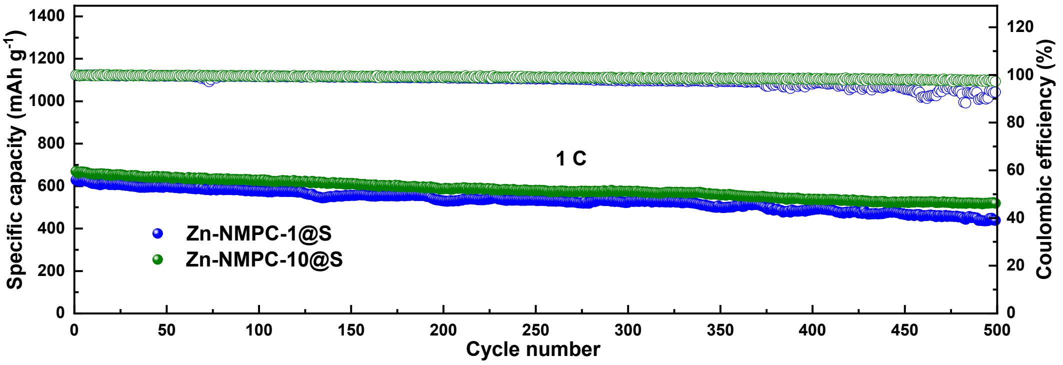

Fig. S17. The long-term cycling performances of the Zn-NMPC-1@S and Zn-NMPC-10@S cathodes at 1.0 C for 500 cycles.

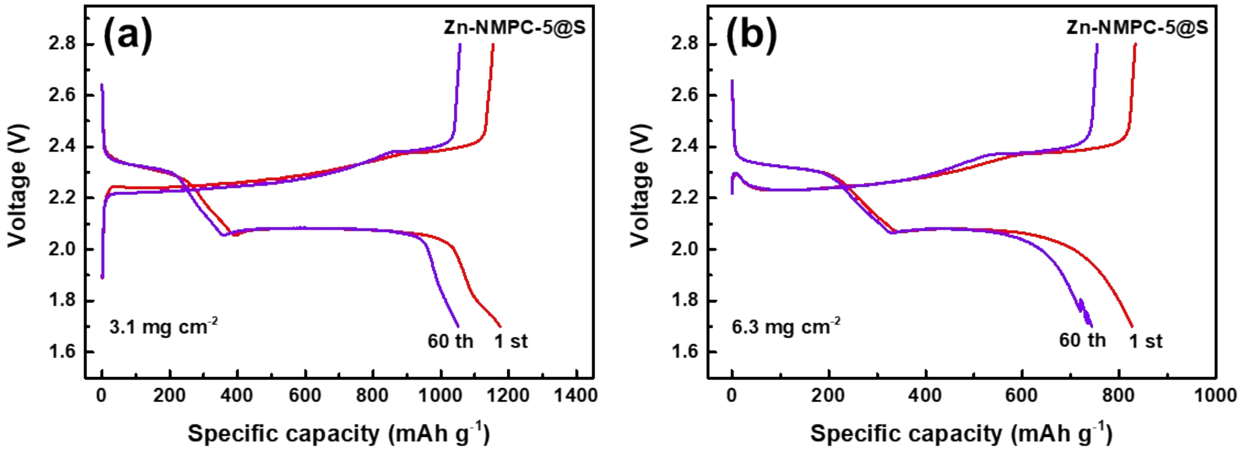

Fig. S18. GCD curve for the Zn-NMPC-5@S with sulfur loadings of (a) 3.1 and (b) 6.3 mg cm−2 at the 1st and 60th cycle (current rate: 0.2 C).

Table S1. Textural parameters of the as-prepared NMPC, Zn-NMPC-1, Zn-NMPC-5, and Zn-NMPC-10 samples.

sample	S_{BET} ($m^2\ g^{-1}$)	V_{total} ($cm^3\ g^{-1}$)	V_{micro} ($cm^3\ g^{-1}$)
NMPC	69.38	0.05	0.03
Zn-NMPC-1	147.41	0.08	0.07
Zn-NMPC-5	161.38	0.10	0.07
Zn-NMPC-10	225.28	0.12	0.10

S_{BET}: Brunauer-Emmett-Teller (BET) specific surface area of as-prepared samples.

V_{total}: the total pore volume of as-prepared samples.

V_{micro}: the microporous volume of as-prepared samples.

Table S2. ICP-OES analysis result of the Zn-NMPC-1, Zn-NMPC-5, and Zn-NMPC-10.

Sample	Element	Element content in solution (mg L^{-1})	Element content in sample (wt.%)
Zn-NMPC-1	Zn	29.39	2.00
Zn-NMPC-5	Zn	24.70	1.22
Zn-NMPC-10	Zn	21.36	1.30

Table S3. ICP-OES analysis result of the Zn-MPC sample.

Sample	Element	Element content in solution (mg L^{-1})	Element content in sample (wt.%)
Zn-MPC	Zn	3.34	0.2

Table S4. A comparison of cycling stability between this work and some other SACs in Li-S batteries reported in previous literature.

Materials	Current rate (C)	Cycle number	Dacay rate (per cycle, %)	Capacity retention rate	Ref.
Zn-NMPC-5@S	1 C	500 cycles	0.026	86.8%	This work
Co-N/G@S	1 C	500 cycles	0.053	73.5%	10
VN_{1-x}@V-NC	1 C	500 cycles	0.047	76.5%	11
Fe-N-C/G@PP	0.5 C	500 cycles	0.053	73.5%	12
Ni@NG	1 C	500 cycles	0.044	78%	13
Co/NDC@S	1 C	500 cycles	0.084	66.6%	14
W/NG@PP	1 C	500 cycles	0.07	65%	15

References

1. G. Kresse and J. Furthmüller, *Physical Review B*, 1996, **54**, 11169-11186.
2. G. Kresse and D. Joubert, *Physical Review B*, 1999, **59**, 1758-1775.
3. J. P. Perdew, K. Burke and M. Ernzerhof, *Phys. Rev. Lett.*, 1996, **77**, 3865-3868.

4. G. Zhou, S. Zhao, T. Wang, S.-Z. Yang, B. Johannessen, H. Chen, C. Liu, Y. Ye, Y. Wu, Y. Peng, C. Liu, S. P. Jiang, Q. Zhang and Y. Cui, *Nano Letters*, 2020, **20**, 1252-1261.
5. C. Ma, Y. Zhang, Y. Feng, N. Wang, L. Zhou, C. Liang, L. Chen, Y. Lai, X. Ji, C. Yan and W. Wei, *Adv. Mater.*, 2021, **33**, 2100171.
6. L. Wang, W. Hua, X. Wan, Z. Feng, Z. Hu, H. Li, J. Niu, L. Wang, A. Wang, J. Liu, X. Lang, G. Wang, W. Li, Q.-H. Yang and W. Wang, *Adv. Mater.*, 2022, **34**, 2110279.
7. J. Wu, T. Ye, Y. Wang, P. Yang, Q. Wang, W. Kuang, X. Chen, G. Duan, L. Yu, Z. Jin, J. Qin and Y. Lei, *ACS Nano*, 2022, **16**, 15734-15759.
8. J. S. Hummelshøj, J. Blomqvist, S. Datta, T. Vegge, J. Rossmeisl, K. S. Thygesen, A. C. Luntz, K. W. Jacobsen and J. K. Nørskov, *J. Chem. Phys.*, 2010, **132**, 071101.
9. X. Wang, J. Yang, S. Liu, S. He, Z. Liu, X. Che and J. Qiu, *Small*, 2023, **20**, 2305508.
10. Z. Du, X. Chen, W. Hu, C. Chuang, S. Xie, A. Hu, W. Yan, X. Kong, X. Wu, H. Ji and L. J. Wan, *J Am Chem Soc*, 2019, **141**, 3977-3985.
11. Y. Zhang, C. Ma, C. Zhang, L. Ma, S. Zhang, Q. Huang, C. Liang, L. Chen, L. Zhou and W. Wei, *Chemical Engineering Journal*, 2023, **452**, 139410.
12. X. Song, S. Wang, G. Chen, T. Gao, Y. Bao, L.-X. Ding and H. Wang, *Chemical Engineering Journal*, 2018, **333**, 564-571.
13. L. L. Zhang, D. B. Liu, Z. Muhammad, F. Wan, W. Xie, Y. J. Wang, L. Song, Z. Q. Niu and J. Chen, *Advanced Materials*, 2019, **31**, 1903955.
14. Y. Wang, C. Shi, J. Sha, L. Ma, E. Liu and N. Zhao, *ACS Appl Mater Interfaces*, 2022, **14**, 25337-25347.
15. P. Wang, B. Xi, Z. Zhang, M. Huang, J. Feng and S. Xiong, *Angewandte Chemie International Edition*, 2021, **60**, 15563-15571.